Kinetic control over droplet ripening in fuel-driven active emulsions

Authors: Marta Tena-Solsona[1,2,+], Jacqueline Janssen[3,4,+], Caren Wanzke[1], Fabian Schnitter[1], Hansol Park[5], Benedikt Rieß[1], Julianne M. Gibbs[5], Christoph A. Weber*[3,4], Job Boekhoven*[1,2]

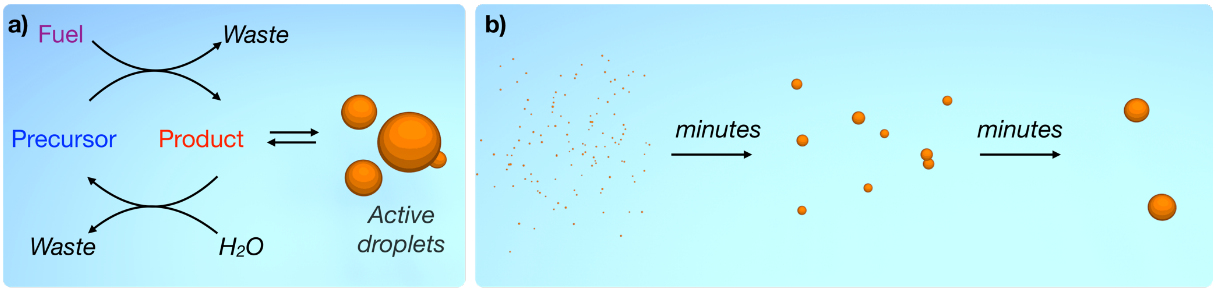

Affiliations:

[1] Department of Chemistry, Technical University of Munich, Lichtenbergstrasse 4, 85748 Garching, Germany.

[2] Institute for Advanced Study, Technical University of Munich, Lichtenbergstrasse 2a, 85748 Garching, Germany.

[3] Max Planck Institute for the Physics of Complex Systems, Nöthnitzer Strasse 38, 01187 Dresden, Germany.

[4] Center for Systems Biology Dresden, Pfotenhauerstrasse 108, 01307 Dresden, Germany.

[5] Department of Chemistry, University of Alberta, 11227 Saskatchewan Drive, T6G 2G2, Edmonton, Canada.

+ These authors contributed equally to this work.

Contact information:

*job.boekhoven@tum.de

*weber@pks.mpg.de

Abstract

Active droplets are made of phase-separated molecules that are activated and deactivated by a metabolic reaction cycle. Such droplets play a crucial role in biology as a class of membrane-less organelles. Moreover, theoretical studies show that active droplets can evolve to the same size or spontaneously self-divide when energy is abundant. All of these exciting properties, *i.e.,* emergence, decay, collective behavior, and self-division, are pivotal to the functioning of life. However, these theoretical predictions lack experimental systems to test them quantitively. Here, we describe the synthesis of synthetic active droplets driven by a metabolic chemical cycle and we find a surprising new behavior, *i.e.,* the dynamics of droplet-growth is regulated by the kinetics of the fuel-driven reaction cycle. Consequently, these droplets ripen orders of magnitude faster compared to Ostwald ripening. Combining experiments and theory, we elucidate the underlying mechanism, which could help better understand how cells regulate the growth of membrane-less organelles.

Active emulsions are crucial for the spatial and temporal organization of the biochemistry in living cells.[1] The droplets in these active emulsions, referred to as membrane-less organelles, can compartmentalize chemical reactions,[2,3] store genetic material,[4] and protect proteins from misfolding in response to environmental stress.[5] Chemical cues within the cell actively control the formation and properties of these droplets.[6,7] For example, the process of activation of the main constituent proteins of P-granules[8] or stress granules[5] involves a metabolic chemical reaction cycle fueled by the hydrolysis of ATP. Due to the combination of phase-separated droplets and fuel-driven chemical reactions, these systems are called active emulsions.[9] Theoretical studies have shown that droplets in such active emulsions exhibit a set of different properties compared to emulsions approaching thermal equilibrium. For example, the droplet size within active emulsions can be regulated by the kinetics of the chemical reactions.[10,11] Similarly, the droplet position and the position of particles within the droplets can be controlled.[12,13,14] Finally, theoretical studies have shown that active droplets can spontaneously divide.[15,16] However, these theoretical predictions lack experimental systems to test them quantitively. Examples of synthetic molecular assemblies regulated by fuel-driven reaction cycles have been described, including chemically[17] and photo-chemically fueled fibers,[17–20] dynamic vesicles formed by the consumption of ATP,[21] and dynamic DNA-based assemblies[22] and colloids.[23] Indeed, such studies result in surprising behavior like dynamic instabilities in synthetic fibers[25] or solutions of nanostructures that oscillate between different colors.[26] However, the field of chemically fueled active droplets remains mostly unexplored from an experimental perspective.[27] Experimental systems of active emulsions could validate theoretical predictions, demonstrate new physical and chemical behavior, and offer valuable insights into the mechanisms relevant for the regulation of membrane-less organelles.

In this work, we have developed synthetic active emulsions regulated by fuel-driven reaction cycles (Fig. 1a). The droplets in these emulsions spontaneously emerge when chemical fuel is supplied, and they decay when all fuel is depleted. These active droplets show a surprising behavior, *i.e.,* the ripening rate is regulated by the kinetics of the reaction cycle (Fig. 1b). The ripening shows similarities to Ostwald ripening (the process in which large droplets grow at the expense of small ones) but is up to two orders of magnitude faster. By the quantitative agreement between experiments and theory, we propose a mechanism for the accelerated ripening. This mechanism may shine new light on how the growth and size of membrane-less organelles are regulated, and may open new doors of controlling nano-structures out-of-equilibrium.

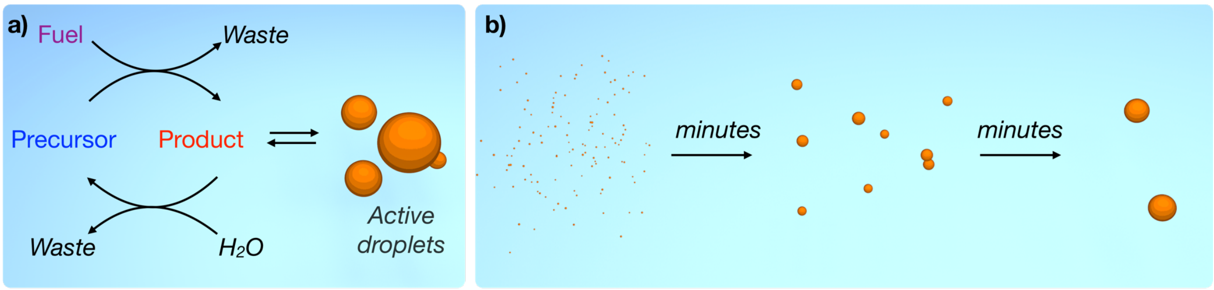

Fig. 1. Schematic representation of active droplet formation. **a)** A chemical reaction cycle drives the transition from the precursor to droplet-forming product at the expense of a chemical fuel (activation). The droplet-forming molecules are unstable and will hydrolyze to the precursor (deactivation). **b)** Schematic representation of the experimentally observed ripening of active droplets. Within minutes, many small drops ripen to a few large ones.

Results and discussion.

Design of the reaction cycle. All active emulsions in this work follow the same design (Fig. 1), *i.e.,* a water-soluble precursor molecule is activated by an irreversible reaction with a fuel.[28] The product of that reaction is less soluble and phase-separates into droplets. Moreover, this product is intrinsically unstable and is spontaneously deactivated via hydrolysis yielding the original precursor. That means that the emergence and sustenance of the active emulsion require fuel, while the phase-separated droplets will decay and vanish in the absence of fuel. Thus, these droplets are active and represent state far away from thermodynamic equilibrium. Because the water-soluble fuel is required for the activation and water is required for the deactivation, the chemical reaction cycle will predominantly take place in the aqueous phase.[23]

We introduce four reaction cycles that are all driven by the hydrolysis of 1-ethyl-3-(3-dimethylaminopropyl)carbodiimide (EDC) as a carbodiimide-based fuel but differ vastly in their deactivation rates (Fig. 2a). In all activation reactions, a carboxylate-based precursor is activated by reaction with EDC (fuel). The activated precursor subsequently reacts with a second nucleophile in order to form the phase-separating product. These nucleophiles are an intramolecular carboxylate to form a cyclic anhydride (Cycle 1 and Cycle 2), an intermolecular carboxylate to form the symmetric anhydride (Cycle 3) or NHS to form the NHS-ester (Cycle 4). The deactivation reaction of the metastable products occurs via hydrolysis of the product. We chose these cycles because of their drastically different hydrolysis rate constant, which scales over three orders of magnitude (*vide infra*). The varying rate constants allow, for the first time, an exploration of the effects of chemical rates on the behavior of an active assembly, *i.e.,* the behavior of the active droplets.

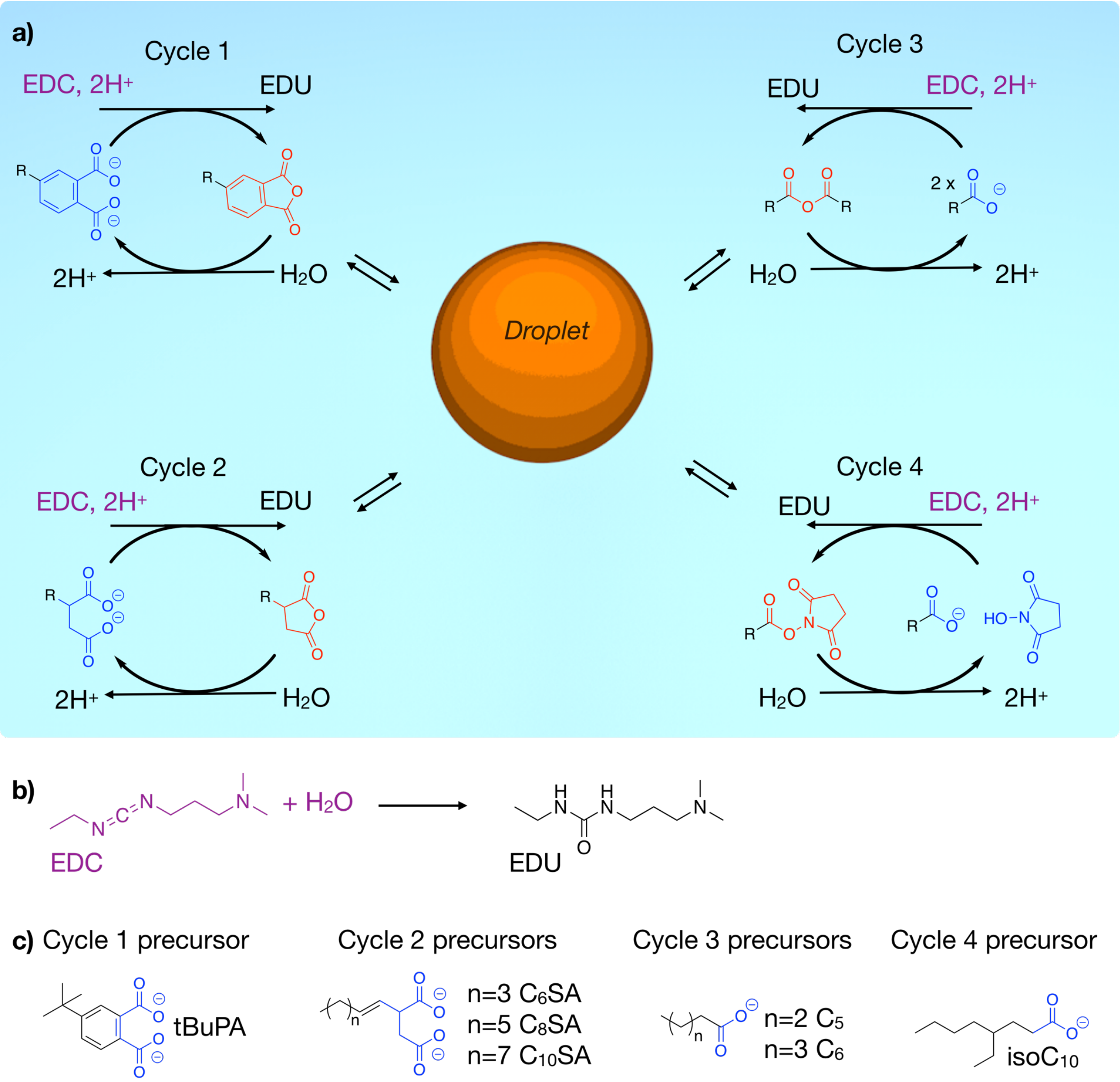

Fig. 2. Chemical reaction cycles leading to an active emulsion. a) *Four chemical reaction cycles that cause the formation of an active emulsion. Each reaction cycles forms a hydrophobic product that phase-separates from water leading to oily, product-rich droplets.* ***b)*** *All reaction cycles are driven by the hydrolysis of EDC.* ***c)*** *List of precursors used for each cycle.*

Molecular design of the precursor. The chemical reaction cycles depicted in Fig. 2a were used to form active emulsions by the hydrolysis of EDC (Fig. 2b). The precursors in each of the reaction cycles (Fig. 2c) follow a simple molecular design. One domain (depicted in black) consists of a linear or branched aliphatic tail that drives phase-separation. The second domain (in blue) is the reactive domain that comprises one or two carboxylate-groups that makes the precursor well soluble. The loss of the negatively charged carboxylate(s) upon the activation reaction (anhydride or NHS-ester formation) results in a decrease in solubility inducing the formation of the active emulsion. Taken together, the chemical reaction cycles convert well-soluble precursor molecules into phase-separating metastable products.

Reaction kinetics with active droplets. For each of the seven precursors depicted in Fig. 2c, we followed the evolution of the reaction cycle in response to a single batch of the fuel (EDC) by measuring the concentration of precursor, product and fuel by HPLC (Fig. 3a-b and Supplementary Fig. 2). In all cases, we found that the concentration of the metastable product initially rises, but decays as the system was running out of fuel. For example, when we added 10 mM EDC to 10 mM C_8SA, we found the maximum product concentration was reached in 20 minutes, after which it decreased to zero. We can thus define a growth- and a decay-regime for each of these experiments. In the growth regime, activation dominates and the product concentration increases. In contrast, in the decay-regime, fuel is depleted, and deactivation dominates.

It should be noted that, for each cycle we tested, the concentration of droplet-forming molecules decayed linearly throughout the decay-regime when droplets were present (Fig. 3b and Supplementary Fig. 2). The linear decay is a result of the constant deactivation rate (hydrolysis) which is induced by a self-protection mechanism of the droplets.[27] Because the droplets do not contain water, the deactivation can take place at the interface of a droplet and on the product fraction that remains in the aqueous phase (*i.e.*, outside of the droplets), which is close to the solubility ($c_{\mathrm{out}}^{(0)}$). The deactivation can thus be described by the effective rate: $r_{\mathrm{eff}} = k_{\mathrm{d}}\, c_{\mathrm{out}}^{(0)}$. We determined the linear deactivation rate (r_{eff}) and the solubility ($c_{\mathrm{out}}^{(0)}$) for all products (Supplementary Table 2). The combined data allows calculating the deactivation rate constant (k_{d}) of each of the products, which scale over two orders of magnitude from $8.2.10^{-3}$ sec^{-1} to $4.9.10^{-5}$ for cycle 1 to cycle 4, respectively (Supplementary Table 2).

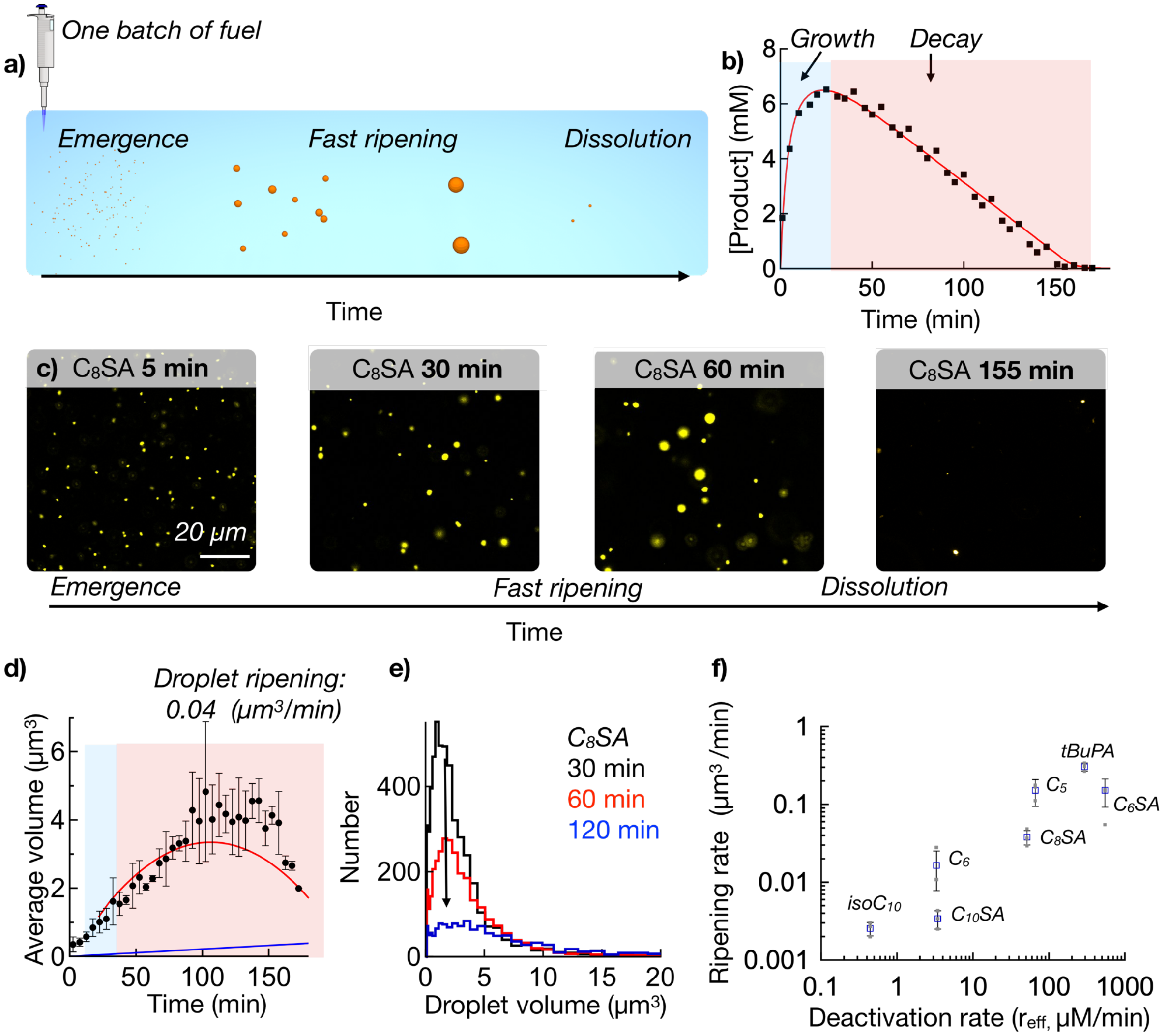

Fig. 3. ***Behavior of batch-fueled active droplets. a)*** *Schematic overview of the experiment: droplets emerge, ripen and dissolve in response to a batch of fuel.* ***b)*** *Total product concentration against time when 10 mM EDC is added to 10 mM C_8SA. Markers represent data measured by HPLC; the solid red line represents the calculated concentrations using our theoretical model. The growth- and decay-regime are shaded blue and red, respectively.* ***c)*** *Micrographs at several time-points in the cycle described in* ***b***. ***d)*** *The average droplet volume against time for the system described in* ***b*** *as measured by image analysis software. The error bar shows the standard deviation for three experiments (N=3). The solid red and blue line represent calculated data for the active ripening and Ostwald ripening, respectively.* ***e)*** *The distribution of droplet volume at 30, 60 and 120 minutes for the active droplets described in* ***b***. ***f)*** *Average volume growth rates against deactivation rates for all droplet-forming reaction cycles. The individual data points are shown (dots), their average (markers), and the standard deviation from the average (error bars, N=3)*

Accelerated ripening of droplets driven by a single batch of fuel. By confocal microscopy and image analysis software, we measured the size of the droplets in response to a single batch of fuel. To measure how the dynamics of the chemical reaction cycle affect the behavior of the droplets, we performed these experiments on all products listed in Fig. 2c, *i.e.*, the active droplets formed by seven precursor-product combinations with vastly different reaction kinetics. We found that for all products, the average volume of the droplets increased throughout most of the experiment. That included the growth-regime, but surprisingly, also the decay-regime in which the total product concentration was decreasing. For example, when we fueled 10 mM C_8SA with 10 mM of fuel, we found the average volume of the droplets increased for the first 140 minutes with an average rate of 0.04±0.009 μm^3/min to almost 5 μm^3 (Fig. 3c-d). After roughly 120 minutes, the droplet volume rapidly decreased, and the droplets disappeared (Fig. 3d). It is important to note that for all droplet forming systems in the growth- or decay-regimen, no droplet fusions were observed. Sporadically, droplets collided and appeared stuck to one another, but they would eventually unstick.

Interestingly, we found that the higher the deactivation rate, the greater the droplet ripening rate, which suggests a relation between the droplet reaction kinetics and its surprising behavior (Fig. 3f, and Supplementary Table 2). For example, 4-tert-butylphthalic anhydride was one of the fastest deactivating products with a hydrolysis rate of 294 μM/min. In the decay-regime, its droplets grew with a rate of 0.30±0.03 μm^3/min (n=3). That means that throughout the 25-minute experiment, droplets emerged and grew to a size of over 6 μm^3 after which they rapidly dissolved (Supplementary Fig. 3). In contrast, the droplets of one of the slowest hydrolyzing anhydrides, $C_{10}SA$ (3.4 μM/min), grew slowly at 0.003±0.001 μm^3/min (n=3). The trend of increasing droplet growth rate with increasing deactivation rate was observed for hydrolysis rates ranging from 0.4 (iso-C_{10}) to 546 μM/min (C_6SA), *i.e.*, over three orders of magnitude.

The histograms of the droplet population at different times in the cycle provided clarity on the surprising average droplet growth (Fig. 3e and SI4). The average volume of droplets increased because small droplets decayed faster than big ones. The loss of small droplets is particularly obvious when plotting the total number of droplets against time, which rapidly decayed (Supplementary Fig. 3). The behavior of average population growth at the expense of small droplets shows some reminiscence to Ostwald ripening.[29] Ostwald ripening is a slow process that relies on diffusion of droplet molecules from small droplets to large ones driven by a shallow concentration difference among droplets. As a result, small droplets decay, while big ones grow (*vide infra,* Fig. 5b). While we observed the decay of small droplets, we did not find the growth of large ones in our experiments. Moreover, the average ripening of the active droplets was fast. To put that in perspective, we measured the ripening rates and compared them to the rates one would expect based on classical Oswald ripening[30] (Supplementary Table 3). We found that the ripening rate is accelerated for all active emulsions and that the acceleration of the ripening more pronounced with increasing hydrolysis rate constant. For example, the ripening rate for the slowest hydrolyzing active emulsion (iso-C_{10}) was accelerated by only a 1.2-fold. In contrast, the ripening rate for C_8SA was 19 times faster than one would expect based on classical Ostwald ripening. The fastest ripening droplets were formed by 4-tert-butylphthalic anhydride which were ripening a 95-fold faster compared to Ostwald ripening.

Accelerated ripening of droplets driven by a continuous supply of fuel. In the experiments above, a finite amount of fuel was initially added as a batch resulting in transient active droplets that ripen rapidly. Such experiments contrast living systems where fuel levels are continuously maintained, and reaction cycles may reach a steady-state, *i.e.,* activation equals deactivation.[31] To test whether the ripening kinetics can also be accelerated when chemical reaction cycles are in a steady-state, we used a reaction-diffusion model to calculate the flux of fuel required to reach steady-states (Supplementary equation (19) for an estimate). To avoid the need of stirring the sample, which would likely affect droplet behavior, we applied a batch of fuel every several minutes and homogenized the sample by shaking it briefly (Fig. 4a). We used HPLC to confirm the formation of the steady-state in the concentration fuel and product (Fig. 4b and S4).

We found that active droplets in a steady-state also ripened rapidly (Fig. 4c-d). Moreover, the active droplets ripened faster compared to the droplets that were batch-fueled (Supplementary Table 3). For example, when C_8SA was brought to steady-state of roughly 7 mM by addition of 4 mM of EDC/hr, the droplet population ripened as fast as 0.11±0.02 μm^3/min (Fig. 4c-e). That means that the average volume growth in steady-state is almost three times faster compared to the batch-fueled experiments and more than 60 times faster compared to classical Ostwald ripening (Supplementary Table 3). The rapid droplet ripening was further confirmed for other active droplet systems in a steady-state, like C_6SA and C_{10}SA (Fig. 4c). We found in experiments that the ripening rate scaled linearly with the deactivation rate of the reaction cycle (Fig. 4f). For C_6SA, the rate was the highest with almost 0.6± 0.2 μm^3/min. Such a growth rate means that droplets had reached an average volume of 15 μm^3 after a two-hour experiment. In contrast, the lower steady-state dynamics of the C_{10}SA droplets resulted in a much slower droplet ripening.

The size distributions of the droplets as a function of time revealed that additional effects were involved in the ripening of droplets in steady-state compared to droplets that were fueled with a single batch. In the batch-fueled experiments, small droplets were decaying faster compared to Ostwald ripening, but large droplets were not growing significantly (Fig. 3e). In contrast, in the continuously-fueled experiments, large droplets were growing while small droplets were decaying fast (see Fig. 4e). The combination of the rapid growth of large droplets and fast decay of small ones further accelerated the ripening compared to batch-fueled experiments.

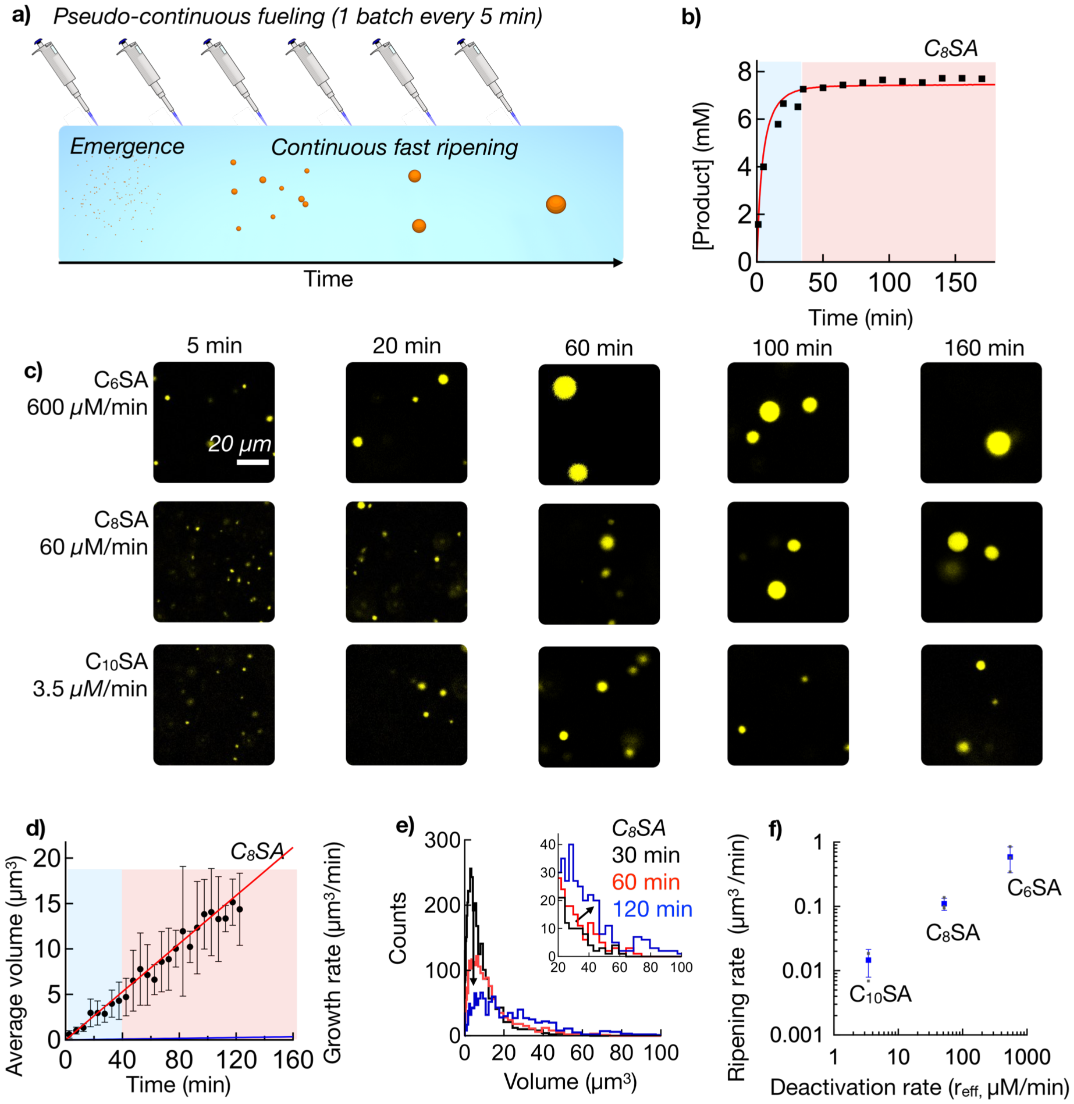

Fig. 4. Behavior of active droplets in a steady-state. a) *Schematic overview of the experiment: droplets emerge and continuously ripen when continuously-fueled by batches of fuel.* ***b)*** *Concentration profile of total product concentration measured by HPLC approaching a steady. Droplet formation was induced by an initial batch of fuel (10 mM EDC to 10 mM C_8) and the system was maintained in steady-state by continuously fueling with 4 mM EDC/hr. Markers represent data measured by HPLC; the solid red line represents the calculated concentrations using our theoretical model. The growth- and steady-state-regime are shaded blue and red, respectively.* ***c)*** *Micrographs of active droplets of C_6SA, C_8SA and C_{10}SA in a steady-state by continuous addition of fuel.* ***d)*** *Average droplet volume over time for experiment discussed in* ***a.*** *The solid red and blue line represent calculated data for the active ripening and Ostwald ripening, respectively.* ***e)*** *The distribution of droplet volume at 30, 60 and 120 minutes for the active droplets described in* ***a.*** ***f)*** *Droplet ripening rates against the deactivation rate. The individual data points are shown (dots), their average (markers), and the standard deviation from the average (error bars, N=3).*

Theoretical model of accelerated ripening. To understand the mechanism of accelerated ripening, we derived a reaction-diffusion model that can quantitatively describes how the reaction cycle affects the droplet ripening. Our model accounts for phase-separation between product and solvent, diffusion, and all chemical reactions (see Supplementary Information for details on the model). Numerical solutions to the model show a good agreement with the concentrations of fuel and total product concentration measured by HPLC indicating that the model can quantitatively capture the coupling between phase-separation and reaction kinetics (Fig. 3b, 4b, S2, S4). Besides, we reduce the reaction-diffusion equations using conditions that are consistent with the experiments and derive an explicit mathematical expression for the average volume of droplets with time (Supplementary Equation (28, 29)). This expression involves the physical and chemical reaction parameters of the system which we have determined for each emulsion and chemical reaction cycle (*e.g.*, interfacial surface tension, solubility and rate constants, see Supplementary Table 2). We find that our theoretical model leads to an average droplet volume with time which coincides well with the measurements (red lines in Fig. 3d, 4d, and Supplementary Fig. 3 and 5).

The agreement between experiment and theory suggests that the mechanism of the rapid ripening is based on a combination of Ostwald ripening and the fuel-driven reaction cycle. Ostwald ripening occurs because smaller droplets have a greater Laplace pressure compared to large droplets. This difference in Laplace pressures leads to a slightly higher concentration of droplet molecules around small droplets compared to large ones (Fig. 5a). Consequently, a diffusive flux of the droplet molecules from small to big droplets is established which scales with the surface tension. This diffusive flux drives the slow growth of the bigger droplets at the expense of smaller shrinking ones which eventually dissolve (Fig. 5b).

In our active emulsion, a similar concentration gradient emerges between small and big droplets (Fig. 5c). However, besides the diffusive flux between droplets, the chemical kinetics of product activation and deactivation also play a role in how product molecules are distributed between droplets. We first describe how product deactivation accelerates droplet ripening because it is the predominant chemical reaction that occurred in the experiments fueled by a single batch of fuel. The deactivation occurs in the aqueous phase between the droplets and can create a local undersaturation, *i.e.,* upon deactivation, the local concentration is slightly lowered below the solubility concentration of the product (Fig. 5c). That local undersaturation is rapidly restored via diffusion of product molecules from one of the surrounding droplets. However, because of the concentration gradient between small and large droplets, the local undersaturation is more likely to be “filled” by products expelled from a small droplet. Deactivation thus increases the efflux from the small droplets compared to Ostwald ripening resulting in accelerated decay of small droplets. Consequently, this acceleration of ripening is regulated by the kinetics of the deactivation: the faster the deactivation, the faster the ripening (Fig. 3f). Finally, once droplets numbers are low and the droplets are on average far apart, diffusion cannot catch up with the deactivation reaction.

Consequently, droplets quickly dissolve, and the system becomes homogeneous, which we observed experimentally (Fig. 3c-d).

In the case of continuous fueling, both deactivation and activation affect the ripening of droplets. That means that small droplets dissolve faster compared to Ostwald ripening because of the mechanism discussed above (Fig. 5c). Besides, the activation continuously produces product between the droplets leading to a local higher supersaturation (Fig. 5d). This increase of supersaturation is more likely to be “absorbed” by a large droplet rather than by a small one because products diffuse down the concentration gradient. The combined mechanism implies an accelerated decay of small droplets (*via* deactivation) and accelerated growth of large droplets (*via* activation). Interestingly, the simultaneous occurrence of both phenomena is visible in the evolution of the histograms, *i.e.*, the population of small droplets vanishes, while the population of large droplets grows (Fig. 4e).

The proposed mechanism explains that ripening is accelerated compared to Ostwald ripening because droplet material is deactivated in the batch-fueled experiments, or both activated and deactivated in the continuously fueled experiments. The mechanism also explains the difference in ripening rates between the two fueling protocols, *i.e.,* ripening is fastest when continuously fueled (Fig. 5e). Our theory suggests that a combination of parameters (deactivation rate, solubility, surface tension, and molecular volume) determine the faster ripening compared to Ostwald ripening (Supplementary Equation (30)). We combine these parameters into a rescaled effective deactivation rate such that it represents an effective parameter that determines the ripening rate compared to Ostwald ripening. We plot the degree of acceleration compared to Ostwald ripening, *i.e.,* the measured ripening rates divided by the theoretical Ostwald ripening rates, as a function of this rescaled deactivation rate (Fig. 5f), and find excellent agreement between experimental data and theory. From this plot, it becomes clear that the ripening of iso-C_{10}, with the lowest rescaled deactivation rate, is almost exclusively driven by Ostwald ripening. In contrast, tBuPA is accelerated by almost two orders of magnitude compared to Ostwald ripening due to its large deactivation rate constant. Finally, the plot demonstrates that continuously fueled active emulsions will ripen faster than batch-fueled emulsions by a factor of 2-5.

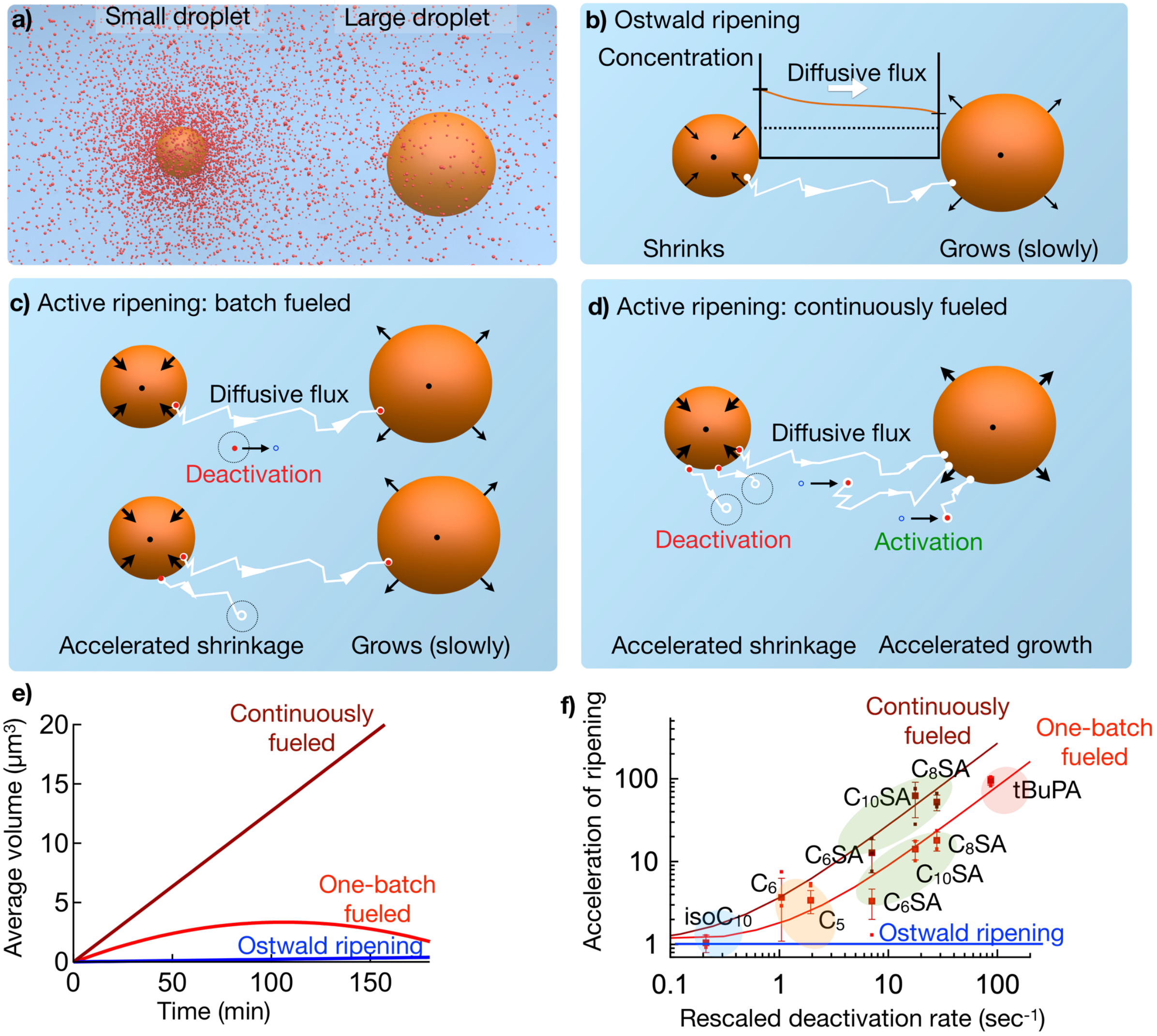

Fig. 5. Mechanism of active ripening. a) *Schematic representation of product molecules (red sphere) around a small droplet (left orange sphere) and large droplet (right orange sphere). Due to a different Laplace pressure, a small droplet is surrounded by a higher concentration of product than a large droplet.* ***b)*** *Due to the concentration gradient described in* ***a****, molecules diffuse from small to large droplets. Consequently, the droplet population ripens, i.e., big droplets grow, while small drops decay.* ***c)*** *In the case of active ripening, the deactivation reaction increases the efflux from small droplets.* ***d)*** *In the presence of fuel, the activation of product leads to an additional faster growth of large droplets compared to* ***c****.* ***e)*** *Theoretically calculated average droplet volumes as a function of time for C_8SA subjected to Ostwald ripening (blue), accelerated ripening when fueled with a single batch (red), and accelerated ripening when fueled continuously (dark red).* ***f)*** *Acceleration of ripening against the rescaled deactivation rate when products are subjected to one batch of fuel (red) or when continuously fueled (dark-red). The products are grouped per reaction cycle (blue for cycle 4, orange for cycle 3, green for cycle 2 and red for cycle 1). The individual data points are shown (dots), their average (markers), and the standard deviation from the average (error bars, N=3).*

Conclusion

In this work, we described a new behavior in active emulsions, *i.e.,* the ripening rate of the droplet population is regulated by the kinetics of the underlying chemical reaction cycle. We designed four chemical reactions cycles with reaction rates that span over three orders of magnitude in order to quantitatively understand the behavior, and we find that the faster the reaction cycle, the greater the acceleration of ripening. Given the simplicity of the mechanism, we anticipate that the behavior can be observed in other fuel-driven assemblies. For example, accelerated growth could be observed in membrane-less organelles, provided that protein activation and deactivation occurs outside of the organelle (*e.g.,* by kinases that operate in the cytosol, but not in the organelle). The mechanism could thus help to explain how the growth of membrane-less organelles is regulated. Moreover, we believe the mechanisms will hold for crystal growth or the synthesis of nanoparticles, which are also subjected to Ostwald ripening. Such accelerated growth will be particularly powerful for the synthesis micro- and nanostructures of tunable size. For example, once an emulsion has reached a certain average droplet size via the accelerated ripening, the droplets can be polymerized.

Methods

Materials. 4-Morpholineethanesulfonic acid (MES) buffer, pentanoic acid, hexanoic acid, 2-hexenyl-succinic anhydride, 2-octenyl-succinic anhydride, 2-decenyl-succinic anhydride, t-butyl-phthalic anhydride, 4-ethyloctanoic acid, 1-Ethyl-3-(3-dimethylaminopropyl) carbodiimide (EDC), N-hydroxysuccinimide (NHS) and Nile Red were all purchased from Sigma-Aldrich and Alfa-Aesar unless indicated otherwise. The precursors C_6SA, C_8SA, C_{10}SA, and isoC_{10}, were synthesized by hydrolysis of their corresponding anhydrides. The anhydrides were suspended in demineralized water and hydrolyzed over 48 hours while stirring the samples. The absence of anhydride was assessed by HPLC. The samples were freeze-dried and stored at -20 ºC until further use. Their purity was assessed by and Electrospray Ionization-Mass Spectroscopy (ESI-MS) and HPLC.

Sample preparation. We prepared stock solutions of the precursors by dissolving it in MES buffer and subsequently adjusting the pH to 6.0. We used 200 mM of MES buffer for precursor concentrations of 10 mM or less. For higher precursor concentrations, we used a buffer concentration of 500 mM. We used the precursors at the following concentrations: 300 mM C_5, 100 mM C_6, 10 mM of C_6SA, 10 mM of C_8SA, 7.5 mM of C_{10}SA, 10 mM of tBuPA, and 5 mM of isoC_{10}. We prepared the stock solutions of EDC by dissolving the EDC powder in demineralized water, typically, at 1.0 M EDC. We initiated the batch-fueled experiments by the addition of various batch-sizes of EDC to the precursor solution. In the case of isoC_{10}, the addition of fuel was accompanied by the addition of 5 mM of NHS. We initiated the continuously fueled experiments by addition of an initial amount of EDC fuel. Specifically, 50 mM of EDC was added to 10 mM of C_6SA; 10 mM of EDC was added to 10 mM C_8SA; 10 mM EDC was added to 7.5 mM of $C_{10}SA$; and 1 mM of EDC (with 5 mM of NHS) was added to isoC_{10}. 15 minutes after the first batch of fuel, EDC was provided with a flux of 55 mM/h, 4 mM/h, 0.6 mM/h and 0.05 mM/h respectively for C_6SA, C_8SA, $C_{10}SA$, and isoC_{10}. We added fuel by four batches of per hour. The mixture was gently shacked after each addition.

Analysis of the kinetics of the chemical reaction cycles. The concentration profiles of the chemical reaction networks were monitored over time by means of analytical HPLC. A 1.5 mL sample was prepared as described above in a screw cap HPLC vial. The reaction solution was stored at 25 ±1°C solution, and samples of the solution were directly injected without further dilution. All reagents in the reaction cycle were separated using linear gradients of water and acetonitrile. See supporting information for more details.

ESI. ESI-MS measurements were performed using a Varian 500 MS LC ion trap spectrometer. The samples were diluted in acetonitrile and injected into an acetonitrile carrier flow (20 µL/min).

Confocal Fluorescence Microscopy. Confocal fluorescence microscopy was performed on a Leica SP5 confocal microscope using a 63x oil immersion objective. Samples were prepared as described above but with 2.5 µM Nile Red as a dye. 12-20 µL of the sample was deposited on the PEG-coated glass slide and covered with a 12-mm coverslip. Every minute a 4096 x 4096 pixel^2 image was acquired of an area that covered 246 µm x 246 µm. Each experiment was performed in triplicate (n=3). More details can be found in the Supporting Information.

Image analysis and droplet volume and growth rate calculations. Images were analyzed with ImageJ's "analyse particles" package, from which we derived the volume of each droplet. We then calculated the average droplet volume per micrograph and binned several micrographs that were taken with one-minute intervals. The standard deviation was calculated between the three replicates of the experiments (*n*=3). From this dataset, the histograms of the droplet distributions were also calculated. We calculated the droplet growth by measuring the slope of the droplet volume over time for each individual experiment. Then, the average growth rate and the standard deviation between the three replicates were calculated (*n*=3). The droplet number was also obtained from the image analysis. Similar to the average droplet volume, the droplet number was obtained by binning all the image analysis droplet data in two-minute bins (for C_5, C_6SA, and tBuPA) and five-minute bins (for C_6, C_8SA, $C_{10}SA$, and isoC_{10}) to ensure a sufficient droplet number per unit of time. The standard deviation was calculated between 3 experiments (*n*=3).

Theoretical model and classical Ostwald ripening. Our reaction-diffusion model accounts for phase-separation and the fuel-driven chemical reactions. The underlying equations have been analyzed numerically and also used to find an explicit expression for the average volume as a function of the experimental parameters (e.g., solubility, surface tension, and diffusion constant). More information can be found in the SI. We also calculated the Ostwald ripening rates of our emulsions based on theory from Lifshitz and Slyozov.[30]

Data availability

The data that support the findings of this study are available from the authors on reasonable request.

Acknowledgments.

J.B. is grateful for funding by the Technical University of Munich – Institute for Advanced Study, funded by the German Excellence Initiative and the European Union Seventh Framework Programme under grant agreement n° 291763. M.T.S. acknowledges the European Union's Horizon 2020 Research and Innovation program for the Marie Sklodowska Curie Fellowship under grant agreement n° 747007. Financial support for C.W. comes from the German Research Foundation (DFG) through Transregional Collaborative Research Center (SFB/Transregio) 235 Project 16.

Author Contributions.

J.B. and M.T.S. designed the experiments. J.J. and C.W. worked out the theory. M.T.S, C. W., F.S., H.P., B.R. J.M.G. carried out the experiments. J.B and C.W. wrote the manuscript.

Competing Interests statement.

The authors declare no competing interests.

References:

1. Alberti, S. Phase-separation in biology. *Curr. Biol.* **27**, R1097–R1102 (2017).
2. Banani, S. F., Lee, H. O., Hyman, A. A. & Rosen, M. K. Biomolecular condensates: organizers of cellular biochemistry. *Nat. Rev. Mol. Cell Biol.* **18**, 285–298 (2017).
3. Stroberg, W. & Schnell, S. Do Cellular Condensates Accelerate Biochemical Reactions? Lessons from Microdroplet Chemistry. *Biophys. J.* **115**, 3–8 (2018).
4. Zhang, H. *et al.* RNA Controls PolyQ Protein Phase Transitions. *Mol. Cell* **60**, 220–230 (2015).
5. Wallace, E. W. J. *et al.* Reversible, Specific, Active Aggregates of Endogenous Proteins Assemble upon Heat Stress. *Cell* **162**, 1286–1298 (2015).
6. Shin, Y. & Brangwynne, C. P. Liquid phase condensation in cell physiology and disease. *Science* **357**, eaaf4382 (2017).

7. Saha, S. *et al.* Polar Positioning of Phase-Separated Liquid Compartments in Cells Regulated by an mRNA Competition Mechanism. *Cell* **166**, 1572-1584.e16 (2016).

8. Brangwynne, C. P. *et al.* Germline P Granules Are Liquid Droplets That Localize by Controlled Dissolution/Condensation. *Science* **324**, 1729–1732 (2009).

9. Weber, C. A., Zwicker, D., Jülicher, F. & Lee, C. F. Physics of active emulsions. *Rep. Prog. Phys.* **82**, 064601 (2019).

10. Zwicker, D., Hyman, A. A. & Jülicher, F. Suppression of Ostwald ripening in active emulsions. *Phys. Rev. E* **92**, (2015).

11. Wurtz, J. D. & Lee, C. F. Chemical reaction-controlled phase-separated drops: Formation, size selection, and coarsening. *Phys. Rev. Lett.* **120**, 078102 (2018).

12. Weber, C. A., Lee, C. F. & Jülicher, F. Droplet ripening in concentration gradients. *New J. Phys.* **19**, 053021 (2017).

13. Krüger, S., Weber, C. A., Sommer, J.-U. & Jülicher, F. Discontinuous switching of position of two coexisting phases. *New J. Phys.* **20**, 075009 (2018).

14. Zwicker, D. *et al.* Positioning of Particles in Active Droplets. *Phys. Rev. Lett.* **121**, 158102 (2018).

15. Zwicker, D., Seyboldt, R., Weber, C. A., Hyman, A. A. & Jülicher, F. Growth and division of active droplets provides a model for protocells. *Nat. Phys.* **13**, 408–413 (2017).

16. Seyboldt, R. & Jülicher, F. Role of hydrodynamic flows in chemically driven droplet division. *New J. Phys.* **20**, 105010 (2018).

17. Leira-Iglesias, J., Sorrenti, A., Sato, A., Dunne, P. A. & Hermans, T. M. Supramolecular pathway selection of perylenediimides mediated by chemical fuels. *Chem. Commun.* **52**, 9009–9012 (2016).

18. Boekhoven, J. *et al.* Dissipative Self-Assembly of a Molecular Gelator by Using a Chemical Fuel. *Angew. Chem. Int. Ed.* **49**, 4825–4828 (2010).

19. Sorrenti, A., Leira-Iglesias, J., Sato, A. & Hermans, T. M. Non-equilibrium steady-states in supramolecular polymerization. *Nat. Commun.* **8**, 15899 (2017).

20. Debnath, S., Roy, S. & Ulijn, R. V. Peptide Nanofibers with Dynamic Instability through Nonequilibrium Biocatalytic Assembly. *J. Am. Chem. Soc.* **135**, 16789–16792 (2013).

21. Maiti, S., Fortunati, I., Ferrante, C., Scrimin, P. & Prins, L. J. Dissipative self-assembly of vesicular nanoreactors. *Nat. Chem.* **8**, 725–731 (2016).

22. Heinen, L. & Walther, A. Programmable dynamic steady-states in ATP-driven nonequilibrium DNA systems. *Sci. Adv.* 9 (2019).

23. Rieß, B. *et al.* Dissipative assemblies that inhibit their deactivation. *Soft Matter* **14**, 4852–4859 (2018).

24. Kariyawasam, L. S. & Hartley, C. S. Dissipative Assembly of Aqueous Carboxylic Acid Anhydrides Fueled by Carbodiimides. *J. Am. Chem. Soc.* **139**, 11949–11955 (2017).

25. Boekhoven, J., Hendriksen, W. E., Koper, G. J. M., Eelkema, R. & van Esch, J. H. Transient assembly of active materials fueled by a chemical reaction. *Science* **349**, 1075–1079 (2015).

26. Leira-Iglesias, J., Tassoni, A., Adachi, T., Stich, M. & Hermans, T. M. Oscillations, travelling fronts and patterns in a supramolecular system. *Nat. Nanotechnol.* **13**, 1021–1027 (2018).

27. Tena-Solsona, M., Wanzke, C., Riess, B., Bausch, A. R. & Boekhoven, J. Self-selection of dissipative assemblies driven by primitive chemical reaction networks. *Nat. Commun.* **9**, 2044 (2018).

28. Tena-Solsona, M. *et al.* Non-equilibrium dissipative supramolecular materials with a tunable lifetime. *Nat. Commun.* **8**, 15895 (2017).

29. Voorhees, P. W. Ostwald Ripening of Two-Phase Mixtures. 20

30. Lifshitz, I. M. & Slyozov, V. V. The kinetics of precipitation from supersaturated solid solutions. *J. Phys. Chem. Solids* **19**, 35–50 (1961).

31. Alberts, B. *Molecular biology of the cell.* (Garland Science, Taylor and Francis Group, 2015).